Characterization of manganese-bearing particles in the vicinities of a manganese alloy plant

Ana Hernández-Pellón, Ignacio Fernández-Olmo, Frédéric Ledoux, Lucie Courcot, D. Courcot

Accepted Manuscript

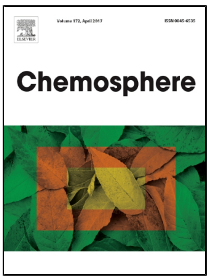

Characterization of manganese-bearing particles in the vicinities of a manganese alloy plant

Ana Hernández-Pellón, Ignacio Fernández-Olmo, Frédéric Ledoux, Lucie Courcot, Dominique Courcot

PII:	S0045-6535(17)30234-5
DOI:	10.1016/j.chemosphere.2017.02.056
Reference:	CHEM 18819
To appear in:	*Chemosphere*
Received Date:	30 December 2016
Revised Date:	08 February 2017
Accepted Date:	09 February 2017

Please cite this article as: Ana Hernández-Pellón, Ignacio Fernández-Olmo, Frédéric Ledoux, Lucie Courcot, Dominique Courcot, Characterization of manganese-bearing particles in the vicinities of a manganese alloy plant, *Chemosphere* (2017), doi: 10.1016/j.chemosphere.2017.02.056

Highlights

- Most of the particles collected in an urban area near a Mn alloy plant contain Mn
- PM_{10} is mainly composed of Si-Mn particles with spherical shapes and small sizes
- Mn-bearing particles in deposition samples are mostly attributed to alloys and slags
- Mn solubility is expected to be higher in PM_{10} compared to deposition samples

CHARACTERIZATION OF MANGANESE-BEARING PARTICLES IN THE VICINITIES OF A MANGANESE ALLOY PLANT

Ana Hernández-Pellón[a*], Ignacio Fernández-Olmo[a], Frédéric Ledoux[b], Lucie Courcot[c], Dominique Courcot[b]

[a] Dpto. de Ingenierías Química y Biomolecular, Universidad de Cantabria, Avda. Los Castros s/n, 39005 Santander, Cantabria, Spain
[b] Unité de Chimie Environnementale et Interactions sur le Vivant (UCEIV, EA4492), Université du Littoral Côte d'Opale, 145 avenue Maurice Schumann, 59140 Dunkerque, France
[c] Laboratoire d'Océanologie et de Géosciences (LOG, CNRS UMR8187), Université du Littoral Côte d'Opale, Wimereux, France

[*]Corresponding Author
Dpto. de Ingenierías Química y Biomolecular, Universidad de Cantabria, Avda. Los Castros s/n, 39005 Santander, Cantabria, Spain
ana.hernandez@unican.es

Abstract

Numerous studies have associated air manganese (Mn) exposure with negative health effects, primarily neurotoxic disorders. Despite there is not a specific European regulation, institutions such as the World Health Organization (WHO) have proposed an annual average guideline value of 150 ng/m^3. Bioaccessibility and toxicity mechanisms of Mn remain unclear, however it is generally agreed that adverse health effects are strongly linked to particle size and morphology, chemical composition and oxidation state. This study aims to deepen the understanding of the physico-chemical characteristics of PM_{10} and deposition samples collected in an urban area in the proximities of a ferromanganese alloy plant. Total Mn content was determined by ICP-MS after a microwave-assisted acid digestion. The size, morphology and chemical composition of individual particles were studied by SEM-EDX. XRD was used to identify the major crystalline phases. Most of the particles observed by SEM-EDX contain Mn. 60% of Mn-PM_{10} particles were spheres of small size and were attributed to condensation processes at the smelting unit. Mn-bearing particles present in deposition were characterized by irregular shapes and bigger sizes, most of them consisting of SiMn slags and Mn ores and alloys, and attributed to diffuse emissions from raw material and product handling and processing. Due to the differences in the characteristics of Mn-bearing particles found in the different matrices, further studies on the

potential toxicity and health effects of these particles should be done, especially in relation with the small and spherical particles present in PM_{10}, which are expected to be more problematic.

Keywords

Manganese, SEM-EDX, XRD, ferroalloy plant, PM_{10}, deposition

1. Introduction

Manganese (Mn) is a trace element considered essential to human health. Due to its catalytic and regulatory function, it plays an important role in several enzyme systems, being therefore required for a wide variety of physiological processes. It is necessary for the metabolic activity, skeletal development, as well as for the maintenance of the nervous and immune systems (Santamaria, 2008). In addition, it contributes to a normal reproductive hormone function and to the prevention of cellular oxidative stress (Freeland-Graves et al., 2015; Keen et al., 2000). Although Mn, as a nutrient, is vital for the human body, it can be toxic as a result of overexposure.

Mn toxicity to humans by inhalation has been widely reported in comparison with other routes of exposure (ATSDR, 2012; WHO, 2000), mainly linked to neurological problems. Chronical occupational exposure can lead to the development of manganism, with some general resemblance to Parkinson's disease (Flynn and Susi, 2009; Kwakye et al., 2015; Park, 2013). Whereas the impacts of Mn exposure in human health have been extensively established in relation with workplaces (Crossgrove and Zheng, 2004), there has only been a growing interest in the last decade about the consequences of Mn chronic exposure in the overall population, especially in susceptible groups like children (Carvalho et al., 2014; Riojas-Rodríguez et al., 2010; Rodríguez-Barranco et al., 2013). In this regard, recent studies suggest that ambient air Mn exposure may also be associated with neurotoxic disorders, including motor and cognitive deficits (Chen et al., 2016; Lucchini et al., 2012; Menezes-Filho et al., 2011; Rodríguez-Agudelo et al., 2006; Roels et al. 2012). Even though negative health effects as a consequence of airborne Mn overexposure have been pointed out, there is no specific European regulation that establishes limit

values for Mn in air. Nevertheless, the World Health Organization (WHO) has proposed an annual average guideline value of 150 ng Mn/m^3.

Mn is an element present in several environmental matrices, however, high concentrations in air are due to anthropogenic sources, one of the most important being the ferromanganese alloy production. According to the WHO criteria, exceedances of Mn concentrations in air have been widely reported in areas close to Mn alloy plants, pointing out that even when PM_{10} levels fulfil the European regulatory limits, Mn should be a cause of concern in locations influenced by the emission from this activity. For instance, Haynes et al. (2010) have reported an annual average concentration of Mn of 203 ng/m^3 at approximately 4.5 miles to the north/north-east of a ferromanganese refinery located in the Marietta community (14,515 inhabitants, USA). Also, an average Mn concentration of 7,560 ng/m^3 in dust collected by global filtration have been reported by Ledoux et al. (2006) in the vicinities of a ferromanganese metallurgy plant located in Boulogne-sur-Mer agglomeration (120,000 inhabitants, France).

Mn levels in air reach 4-23 ng/m^3 in several urban background areas in Spain (Querol et al., 2007), nevertheless annual average concentrations above the WHO guideline have been repeatedly reported in the Region of Cantabria, northern Spain. In Santander, capital of the region (174,000 inhabitants), located 7 km-NE of a ferromanganese alloy plant, an annual average value of 166 ng Mn/m^3 was reported in 2007 (Moreno et al., 2011). Also in 2005 and 2009, annual average levels of 781 ng Mn/m^3 (CIMA, 2006) and 1072 ng Mn/m^3 (CIMA, 2010) respectively, were obtained in the area of Maliaño, a small town with around 10,000 inhabitants where the ferroalloy plant is located. Even though the application of corrective measures in the plant in 2008 led to an improvement of Mn air concentrations in Santander, where mean values of 49.1 ng Mn/m^3 (Arruti et al., 2010) and 31.5 ng Mn/m^3 (Ruiz et al., 2014) were reported in 2008 and 2009, respectively, Mn levels in 2015 still exceeded the WHO recommendation in some areas of Maliaño town, with monthly mean values up to 713.9 ng/m^3 and reaching 3200 ng/m^3 daily Mn concentrations (Hernández-Pellón and Fernández-Olmo, 2016).

Mn emissions to the atmosphere sourcing from ferroalloy plants can exist as aerosols or suspended particulate matter (ATSDR, 2012). Smallest particles will remain suspended for long

periods and then, together with bigger particles, will be deposited by dry or wet deposition. Particulate matter is generated from several activities during ferroalloy production, including raw material handling, sintering, smelting and tapping, casting and product handling (Davourie et al., 2016). Mn ores can be directly introduced into the electrical furnaces or agglomerated with other raw materials such as fluxes and coal in a sintering unit. Figure 1 shows the most common point and fugitive sources of particulate matter (PM) and therefore, potential sources of Mn, in a typical Mn ferroalloy production plant without sintering process. The variety of point and diffuse Mn sources in a ferroalloy plant shown in Figure 1 may lead to the emission of a mixture of Mn-bearing particles with different physico-chemical characteristics.

Even though more efforts should be done in establishing Mn bioaccessibility and toxicity mechanisms (Santamaria, 2008), it is generally agreed that they are strongly linked to particle size and morphology, chemical composition and oxidation state (Majestic et al., 2007). The size distribution of Mn-bearing particles will determine their capability of passing the larynx (thoracic fraction) and ciliated airways (respirable fraction) during inhalation, and therefore could determine their potential health effects. Also, the particle size distribution within the respirable aerosol fraction may have large consequences for the pulmonary Mn absorption (Ellingsen et al., 2013). The predominant oxidation states of Mn found in the inhalable aerosol fraction in FeMn and SiMn plants are Mn^{0} and Mn^{2+}; however, Mn^{3+} and Mn^{4+} have also been previously identified (Thomassen et al., 2001). In addition, particle solubility is important for the systemic uptake of Mn after inhalation. In this regard, a greater association has been found between the more soluble Mn compounds and their presence in biological samples, with respect to insoluble Mn compounds (Ellingsen et al., 2003). Thus, taking into account the variety of emission sources from ferroalloy plants, the study of the physico-chemical characteristics of Mn-bearing particles is essential to better assess their potential health effects.

In the last years, some studies have focused on the assessment of PM toxicity based on its physico-chemical characteristics (Dieme et al., 2012; Megido et al., 2016; Perrone et al., 2010; Rosas Pérez et al., 2007), but only a few studies dealt with the characterization of Mn-bearing particles collected inside or in the vicinities of ferromanganese alloy plants. According to the

literature, dust samples collected in different locations inside ferromanganese alloy plants have been already studied (Figure 1). In particular, PM emissions from the chimneys, e.g., downstream of the industrial filters (Arndt et al., 2016; Marris et al., 2012; Marris et al., 2013), Mn ores (Arndt et al., 2016), as well as samples collected directly from air pollution control devices such as wet scrubbers (Shen et al., 2005) or other industrial filters (Arndt et al., 2016) have been evaluated. In addition, indoor air samplings have been carried out in the factories at different locations: raw materials area (Gunst et al., 2000) and smelting, tapping, ladle and casting area (Gjonnes et al., 2011; Gunst et al., 2000; Kero et al., 2015). Only a few studies focused on the characterization of Mn-bearing particles sampled in residential areas in the vicinities of these plants (Ledoux et al., 2006; Marris et al., 2012; Marris et al., 2013; Moreno et al., 2011).

In the present study, inductively coupled plasma mass spectrometry (ICP-MS), scanning electron microscopy-energy dispersive X ray (SEM-EDX) and X ray diffraction (XRD) have been applied to deepen the understanding of the physico-chemical characteristics of particulate matter and atmospheric deposition in the nearby of a Mn alloy plant located in an industrial-urban area in the Region of Cantabria (northern Spain).

2. Materials and methods

2.1 Area of study

The area of study of this work is located in the north of Spain, in the Region of Cantabria (585,179 inhabitants, 2015), specifically along the Santander Bay. This study has been focused in Maliaño, a town with around 10,000 inhabitants located in the southern part of the Santander Bay, where high concentrations of Mn in ambient air, according to the WHO criteria, have been previously reported (Moreno et al. 2011; Ruiz et al. 2014), identifying the presence of a ferromanganese alloy production plant as the main source of Mn.

This plant, with a total operation area of 174,353 m^2 and a production capacity of 225,000 t/year, specializes in silicomanganese and ferromanganese alloy production, including the manufacturing of three types of ferroalloys: high carbon ferromanganese (FeMn HC), silicomanganese (SiMn) and refined ferromanganese (FeMn MC). Four electric arc furnaces, are

dedicated equally to FeMn HC and SiMn, and an additional furnace is used for FeMn MC production. In the first case, raw materials are fed continuously to the smelting units and, once the process is concluded, tapping is carried out alternatively through one of the two available tap holes, pouring the mixture of molten alloy and slag into a ladle. In this part of the process, molten alloy is separated and transported to the casting area, where it is cooled and solidified, while the slag is sent to the quenching area with the same purpose. Finally, the products are prepared by crushing and screening. Since furnaces producing SiMn are also capable of utilizing the Mn content in FeMn slags, these are reused. FeMn MC manufacture is carried out similarly, but in a discontinuous manner. As shown in Figure 1, furnace off-gas processing at each smelting unit consists primarily of the control of fume emissions by a wet scrubber before flaring off (see A in Figure 1), and an alternative by-pass of the off-gas control equipment to reduce the risk of fire or explosion under certain operation conditions (see B in Figure 1). In addition, a baghouse filter is placed in each smelting building to control the emissions coming from the tapping, ladle and metal casting area (see C in Figure 1). The dust emissions from the ferroalloy crushing and screening are also controlled by baghouse filters.

2.2 Sampling methods

Prior to this work, an intensive PM_{10} sampling campaign was performed in nine sites of Maliaño town. Based on the results of this campaign (i.e. Mn levels), two of the sites with the highest Mn levels were selected to perform a physico-chemical study of manganese-bearing particles: Cros Park (CROS) and "La Vidriera" Cultural Centre (CCV). Sampling locations are shown in Figure 2. Both sites were also chosen due to their closeness to the ferromanganese alloy plant,and for being located in a residential area, downwind of the factory, when the prevailing wind directions in the region are blowing (S-SW). The CROS site (UTM, 30T, X = 431916, Y = 4807982), located at 850 m NNW of the factory is an official monitoring site that belongs to the regional government. On the other hand, the CCV site (UTM, 30T, X= 431899, Y= 4807290) is located at 350 m NNW of the plant, in the rooftop of "La Vidriera" cultural center.

169 PM_{10} samples have been collected by means of low and high volume samplers (2.3 m^3/h and 30
170 m^3/h, respectively) onto polycarbonate and quartz fiber filters. The most suitable sampling time
171 and substrate were chosen considering the analytical technique that will be used next. Firstly, a
172 PM_{10} sampling campaign was performed at CCV site in September 2016 (28 daily samples) with
173 a low volume sampler (2.3 m^3/h) onto Sartorius quartz fiber filters (47 mm) for total metal content
174 analysis. Additionally, some PM_{10} samples were collected at CCV site for SEM observations onto
175 Whatman Nuclepore polycarbonate filters (47 mm, 0.4 μm) with a low volume sampler (2.3
176 m^3/h). These samplings were performed when the prevailing wind in the region was blowing
177 (SSW). Under these wind conditions, the industrial plume sourcing from the ferromanganese
178 alloy plant reaches the CCV site, therefore, these samples are highly influenced by this activity.
179 The sampling time was only 2 h to obtain a suitable dispersion of the particles on the filter.
180 Secondly, an extensive PM_{10} sampling campaign was carried out from January 2015 to January
181 2016 at CROS site (1 sample per week, 52 samples) for total metal content analysis. Some PM_{10}
182 samples with different Mn concentrations were selected for XRD analysis between the 52 daily
183 samples obtained in this campaign. In this case the samples were collected with a high-volume
184 sampler (30 m^3/h) onto Sartorius quartz fiber filters (150 mm). 24 h was a suitable sampling time
185 to get enough amount of particles for the total metal content and XRD analysis. Also, bulk
186 atmospheric deposition samples have been collected monthly from September 2015 to December
187 2016 in CCV site using a funnel and a plastic bottle, based on the European Standard method "EN
188 15841:2009", and then filtered onto Whatman nitrocellulose filters (47 mm, 0.45 μm). Some
189 samples of the insoluble part of the atmospheric deposition were selected for SEM observations
190 and XRD analysis. Finally, a sample of dust was collected on a roof (approximately 10 m a.g.l)
191 at CCV site. The dust was manually sampled with a plastic brush and, subsequently, dried and
192 sieved to obtain two different size fractions: the first one lower than 70 μm (RDa) and the second
193 one ranging from 70-100 μm (RDb). Whereas each deposition sample represents the dust
194 deposited for around a month, the roof dust samples give information about the cumulative dust
195 deposition in the area over a much longer period.

196 2.3 Analytical methodology

197 Total content of Mn and Fe has been determined in PM_{10}, insoluble fraction of atmospheric
198 deposition and roof dust samples, based on the European standard method "EN-UNE 14902-
199 2006". Regarding PM_{10} samples, once gravimetric determination was performed, one part of each
200 filter (a quarter and a half of the quartz fiber filters with 150 mm and 47 mm diameter,
201 respectively) was subjected to microwave assisted acid digestion (HNO_3:H_2O_2 with a mixture of
202 8:2 ml, up to 220ºC) and then the metal content was analyzed by inductively coupled plasma mass
203 spectrometry (ICP-MS, Agilent 7500 CE). Quality control of the analytical procedure included
204 the determination of the recovery values of the analyzed metals in a standard reference material
205 (NIST SRM 1648a, "Urban particulate matter"), as well as the evaluation of the blank
206 contribution from the filters and reagents and subsequent subtraction from the results. For
207 deposition samples half of the nitrocellulose filters (47 mm, 0.45 μm) were cut and the same
208 procedure was applied. Ultimately, around 100 mg of each size fraction of the roof dust sample
209 were also digested and analyzed in duplicate according to the same methodology.

210 Individual particle analysis and SEM images were performed using a LEO 438 VP scanning
211 electronic microscope (LEO Electron Microscopy Ltd, UK) equipped with an Energy Dispersive
212 X-ray spectrometer (IXRF, Oxford Instruments, UK) (SEM-EDX). For the PM_{10} study, particles
213 collected on polycarbonate filter were used. For roof dust and deposition samples, prior to
214 analysis, particles were sonicated in ultrapure water and dispersed over a polycarbonate
215 membrane. For each sample, about 1000 particles were analyzed. Carbon, nitrogen and oxygen
216 ($Z \leq 8$) were not taken into account in this analysis. Each data set was then submitted to
217 hierarchical cluster analysis (HCA) using IDAS, a Windows based software for cluster analysis
218 (Bondarenko et al., 1996); then, similar particles are grouped according to their composition
219 leading to determine the different particle types in the sample.

220 Powder X-ray diffractograms (XRD) were recorded on a BRUKER D8 Advance
221 diffractometer using Cu Kα radiation (λ = 1.5406 Å) in the 2Θ range 10–70◦, with a step size of

0.02° and an integration time of 15 s. Quartz fiber and nitrocellulose filters were used for PM_{10} and deposition samples, respectively. Filters were directly placed on an amorphous holder to record diffractograms. It was verified that both types of filters do not produce any diffraction rays. In all the cases, interpretation was done after baseline correction. Phases identification was performed by comparing the most intense diffraction lines and their relative intensities with the XRD patterns provided by the Joint Committee on Powder Diffraction Standards.

3. Results

3.1 Total metal composition

Table 1 summarizes mean values and standard deviations of Mn and Fe, and the Mn/Fe ratio in PM_{10}, insoluble fraction of atmospheric deposition and roof dust samples. The highest daily Mn level in the 24 h-PM_{10} sampling campaign carried out at CROS site reached 1,279 ng/m^3 with an annual mean value of 231.7 ng/m^3, being 1,018 ng/m^3 and 279.4 ng/m^3 for Fe, respectively. At CCV site the maximum Mn daily concentration was 2,062 ng/m^3 and the monthly mean level was 670.4 ng/m^3, reaching 714.0 ng/m^3 and 322.0 ng/m^3 in the case of Fe, respectively. Even though the annual average guideline value established by WHO (150 ng Mn/m^3) was exceeded in both sites, which are located at NNW from the ferroalloy plant and influenced by the prevailing winds in the region (S/SW), this exceedance was more pronounced at CCV site. The higher Mn level reported in the latter location can be mainly explained due to its greater proximity to the factory and the different meteorological conditions during the performance of the respective sampling campaigns.

Average Mn and Fe concentrations in the insoluble fraction of the atmospheric deposition samples, collected for characterization at CCV site, reached 11,355 and 5,315 μg/m^2·day, respectively. Despite there is no European regulation or recommendations about the Mn level in atmospheric deposition, these values are much higher than the common values obtained in other industrial and urban areas (Ali-Khodja et al., 2008; Castillo et al., 2013; Mijić et al., 2010; Rossini et al., 2010), as well as in other areas of the Cantabria region further away from the factory (Fernández-Olmo et al., 2015).

Regarding roof dust samples, the fraction below 70 µm reached a mean Mn content of 322,507 mg/kg and a Fe content of 159,859 mg/kg, whereas Mn and Fe concentrations in the fraction between 70 and 100 µm were 161,537 mg/kg and 199,517 mg/kg, respectively. Even though these values are much higher than Mn levels found in roof dust samples in other urban or industrial areas (Chattopadhyay et al., 2003; Žibret and Rokavec, 2010; Pavilonis et al., 2015), similar Mn levels have been previously reported in soil samples collected in the direction of the prevailing winds in the vicinities of a ferromanganese alloy plant located in Beauharnois, Canada (Boudissa et al., 2006), even more than 10 years after closure.

As Table 1 shows, the ratio between Mn and Fe in PM_{10} samples is 0.83 and 2.24 in samples collected at CROS and CCV sites, respectively. The higher Mn/Fe ratio found at CCV site can be related to its greater proximity to the factory with respect to CROS site and to the fact that, while the main Mn source throughout the Santander Bay is only attributed to the ferromanganese alloy plant, there are other Fe sources in the area, such as traffic and a steel plant located at around 3 km N from CROS site. Additionally, Mn/Fe ratio in deposition samples collected at CCV site is 2.14, similar to the ratio found in PM_{10} samples at the same location. Finally, the ratio between Mn and Fe content in roof dust samples is 2.02 and 0.81, pointing out the major presence of Mn in the finest dust fraction.

3.2 Characterization of manganese-bearing individual particles

Table 2 shows the types of particles evidenced in PM_{10} samples collected at CCV site using SEM-EDX and after applying the statistical clustering analysis (HCA) (Bondarenko et al. 1996). From this classification, eleven different groups were obtained, corresponding mainly to Mn-bearing particles, Fe-rich particles and aluminosilicates. Particles containing Mn were found in five of these groups: (1P) 21.9 % of particles with Mn, Si and traces of K (Mn/Si ≈0.8), (3P) 12.9 % of particles with Mn and Si (Mn/Si ≈4), (4P) 10.7 % of particles with Mn, Si, Zn and traces of K (Mn/Si ≈0.9), (5P) 10 % of Mn-rich particles and (7P) 4.6 % of particles with Mn, Ca, Si and S (Mn/Si ≈1.5). The most abundant groups containing Mn (1P, 3P and 4P) where mainly spherical particles of small size (mean diameters of 0.67 µm, 0.92 µm and 0.69 µm, respectively)

and were observed either isolated or agglomerated (see Figure 3). Also, more heterogeneous irregular Mn-bearing particles were detected (see 5P and 7P in Figure 3). The second most abundant group determined in the statistical clustering analysis (2P) corresponds to Fe-rich particles with a mean diameter of 1.08 μm. In this case the morphology was not well defined and either spherical or irregular particles were observed.

Some other groups of particles without any Mn content were identified. It can be noted the presence of 9.2 % of particles with Si, Al and S (aluminosilicates) with a mean diameter of 1.77 μm and irregular shapes. Additionally, the following groups were also observed: (8P) 3.5 % of particles containing Fe, Si and S, (9P) 3.3 % of Si-rich particles, (10P) 2.6 % of particles with Ca and S and (11P) 1.9 % of Ca-rich particles. These groups also present an irregular morphology and sizes range from 0.98 to 2.26 μm. Suggested origin of the main clusters will be discussed in more details in the Discussion section.

In relation with deposition and roof dust samples, the SEM-EDX analysis and subsequent statistical clustering analysis (HCA) led to the identification of ten different classes of particles, corresponding mainly to different types of Mn-bearing particles, Fe and Ca-rich particles and aluminosilicates. The relative abundance, mean diameter and composition of these groups are shown in Table 3. The three most abundant groups of particles, all containing Mn, were: (1D) 12 to 41 % of particles composed of Mn, Fe, Si, and Al, (2D) 12-28 % of particles with Si, Ca, Mn, Al, Mg, S and K and (3D) 12-20 % of particles composed of Mn, Si, Fe, Al, Ca, S and Mg. Furthermore, between 7-9 % of particles with similar composition to cluster 2D, but higher Mn content has also been identified (see 5D in Table 3). As it can be seen in Figure 4, particles corresponding to clusters 1D and 3D, with mean diameters of 24.8 μm and 19.9 μm, respectively, show primarily irregular shapes, whereas particles related to cluster 2D (mean diameter, 25.3 μm) appear as angular particles and frequently have holes in their structure. Also, different groups of particles attributed to aluminosilicates, with low Mn content, were observed: (4D) 10-27 % of particles composed of Si, Al, Mn, Fe, Ca, K and S, (8D) 0-7 % composed of Fe, Si, Mn, Al, Ca and S and (9D) 0-2 % of particles with Al, Ca, Mn, S, Si. These three groups of particles, with mean diameters of 13.4 μm, 13.2 μm and 14.6 μm, respectively, are characterized by a smaller

304 size with respect to the most abundant groups containing Mn (1D, 2D and 3D). While particles
305 belonging to cluster 4D were observed in all the analyzed samples, particles from groups 8D and
306 9D only appeared in some of them. Additionally, the following clusters have been observed: (6D)
307 4-7 % of Si-rich, (7D) 2-3 % of Fe-rich and (10D) 0-7 % of Ca-rich. As Figure 4 shows, these
308 groups, with mean diameters of 23.7 μm, 13.0 μm and 9.7 μm, respectively, present also irregular
309 shapes. Cluster suggested origin will be discussed in more details in the Discussion section.

310 3.3 Crystalline phases of manganese-bearing particles

311 Table 4 summarizes the main crystalline phases identified by XRD in PM_{10}, deposition and
312 roof dust samples. The presence of crystalline phases was validated considering at least the two
313 most intense diffraction lines with their relative intensities. In the case of very low intense
314 diffractogram, as for PM_{10} samples, some phases can only be suggested as it was only possible to
315 observe the most intense diffraction line. Nevertheless, these suggested phases were also detected
316 in other published studies dealing with atmospheric particles (Gonzalez et al., 2016; Sturges and
317 Harrison, 1989) or performed at the vicinity of a Mn alloy producer (Marris et al., 2012). As
318 Figure 5 shows, only a few crystallographic phases were identified by XRD in PM_{10} samples. The
319 main Mn-containing phases identified were bixbyite (Mn_2O_3), manganese dioxide (MnO_2) and
320 rhodochrosite ($MnCO_3$). Also, some other compounds without Mn content such as gypsum,
321 quartz, aluminum silicate and calcium carbonate were detected. Figure 6 shows the main
322 crystalline phases identified by XRD in deposition samples. The main Mn-containing phases
323 identified were bixbyite (Mn_2O_3 and $FeMnO_3$), rhodochrosite ($MnCO_3$), manganosite or iron
324 manganese oxide (MnO or $(FeO)_{0.099}/(MnO)_{0.901}$), hausmannite ($Mn_3O_4$), alabandite (MnS),
325 manganese iron silicon (Mn_4FeSi_3), glaucochroite ($(Ca,Mn)_2SiO_4$) and manganocalcite ((Ca,
326 Mn)CO_3). As in the case of PM_{10} samples, quartz and calcium carbonate were also detected by
327 XRD in deposition samples. Additionally, other phases without any Mn content such as
328 microcline ($KAlSi_3O_8$) and dolomite ($CaMg(CO_3)_2$) could also be suggested. Most of the
329 crystalline phases identified in deposition samples, were also observed in roof dust samples,
330 confirming the similar mineralogical identity of both matrices. Only alabandite, was identified in

deposition samples, but not in roof dust samples. Moreover, bustamite and hematite were only detected in the roof dust fraction between 70-100 μm, but not in the fraction below 70 μm, neither in the deposition samples. Also, despite dolomite was found in deposition samples and in the roof dust sample below 70 μm, it was not detected in the fraction between 70-100 μm.

4. Discussion

Around 60% of the particles observed by SEM-EDX in the PM_{10} samples contain Mn. Most abundant groups of Mn-bearing particles (primarily 1P, 3P and 4P) are characterized by spherical shapes and small sizes, most of them in the submicron range, whereas less abundant Mn-clusters (5P and 7P) correspond to heterogeneous irregular particles. Due to the fact that Mn present in inhaled nanoparticles can translocate directly to the brain without entering the lung (Elder et al., 2006; Sunyer, 2008), and taking into account the neurotoxic effect of Mn, further studies in relation with potential toxicity and health effects of such submicron spherical particles should be done. In particular, bioaccessibility studies may be required to assess the health effects of this kind of particles. According to Thomassen et al. (2001), SiMn alloys are almost insoluble; however, Mn^{2+} compounds are easily soluble, and Mn-bearing condensed particles from molten ferroalloy may have been rapidly oxidized. The oxidation of silicomanganese fumes has been pointed by Kero et al. (2015), since oxygen was also detected as major element together with Si and Mn in spherical fume particles collected near a silicomanganese furnace. Gjønnes et al. (2011) also found spherical Mn-rich particles in the FeMn tapping and SiMn casting areas, being ascribed to condensates from the Mn alloy smelting process. Therefore, it can be assumed that the presence of this kind of particles in PM_{10} samples may be due to either diffuse or confined emissions from the ferromanganese alloy smelter building. Main differences between clusters 1P, 3P and 4P are related to Mn/Si ratio and particle size. Whereas cluster 1P and 4P have a Mn/Si ratio of 0.8 and 0.9 respectively, the latter with an important presence of Zn, cluster 3P is characterized by a Mn/Si ratio of 4 and bigger particle size. The greater dominance of Si in the smallest fractions of particles sourcing from the smelting unit process has been previously reported by Kero et al. (2015). Additionally, since a significant presence of Zn has been found in the particles captured by the

baghouse filter that control the dust emissions from the smelting unit in the tapping and casting area (Arndt et al., 2016), it can be assumed that due to the significant amount of Zn in cluster 4P, these particles can be more related to diffuse emissions from the smelting building, resulting from the emissions that are not confined by the hooding system. However, further work should be done to identify the specific origin of these clusters within the process.

Heterogeneous particles with irregular morphology have also been observed, in the literature, in both SiMn and FeMn alloy production, mainly linked to minerals or alloys (Gjønnes et al., 2011; Kero et al., 2015). Bixbyite (Mn_2O_3), manganese dioxide (MnO_2) and rhodochrosite ($MnCO_3$) phases were identified in PM_{10} samples (see Table 4), in agreement with previous observations. Thus, these phases were detected in Mn ores (Arndt et al., 2016; Baioumy et al., 2013), diffuse emissions from the smelting building (Gjønnes et al., 2011), wet scrubber sludge (Shen et al., 2005) or in PM emissions from the smelting unit chimneys (Arndt et al., 2016) (downstream the industrial filters), and therefore, can be attributed to fugitive emissions from Mn ore piles and also to fugitive or confined emissions from the ferromanganese alloy smelter building. In addition, the presence of Mn oxides and carbonates in PM_{10} samples can explain the composition of particles from cluster 5P, since these are Mn rich particles with irregular shapes (it can be recalled that O and C are not detected in the SEM-EDX analysis). As Table 4 shows, and also in accordance with composition of clusters 9P and 11P, some compounds attributed to common raw materials used in the FeMn and SiMn production were identified, primarily quartz and calcium carbonate.

It should also be noted that, since FeMn and SiMn alloys are produced in the plant and both alloys have an important Fe content (≈14-15%), initially, the identification of FeMn particles was expected in PM_{10} samples; however, a cluster with this composition was not found. According to Kero et al. (2015) and Gjønnes et al. (2011) the presence of Fe in the dust sourcing from the SiMn smelting unit is negligible. Moreover, as Gjønnes et al. (2011) reported during production of SiMn, the submicron fraction consists predominantly of SiMn and other Mn-Si particles, whereas in the FeMn production dominates the presence of MnO and minor amounts of other Mn-Fe

385 oxides. Therefore, based on the major presence of Mn-Si particles determined by the SEM-EDX
386 analysis, as well as on the fact that no FeMn cluster was identified, it can be assumed that during
387 the short sampling period for SEM-EDX analysis the production was primarily focused on SiMn
388 alloy.

389 Eight of the ten main groups of particles observed in deposition and roof dust samples by
390 SEM-EDX contain Mn. Particles composed of Mn were bigger with respect to the ones found in
391 PM_{10} samples and have predominantly irregular shapes. The greater variety of Mn bearing
392 particles in deposition samples with respect to PM_{10} samples can be explained by the much longer
393 sampling period, representing many different production scenarios.

394 Based on their morphology and composition, particles from cluster 1D have been attributed
395 to a mixture of FeMn and SiMn alloys. Figure 7 represents the comparison between the
396 composition of cluster 1D, obtained by SEM-EDX, after applying the statistical clustering
397 analysis, and the weighted average relative composition of the alloys taking into account the
398 production pattern throughout the year 2013 (Ferroatlántica, 2013). Despite slight differences
399 between both groups can be observed, particularly in the Si content, this can be attributed to the
400 variability of the production process and it can be assumed that composition of cluster 1D is in
401 general accordance with a mixture of FeMn and SiMn alloys. Therefore, it is likely that particles
402 from group 1D are emitted from activities related to the conversion from molten metal to final
403 Mn alloy product, namely grinding and screening of the alloy. Furthermore, Mn_4FeSi_3 was
404 detected by XRD in all the deposition samples.

405 In parallel, cluster 2D has been attributed to SiMn vitrified slags. First, the morphology of
406 this kind of particles observed in SEM photographs (Figure 4) agrees with the SiMn slags
407 produced by the factory. In addition, according to several authors, SiMn slag is composed mainly
408 of SiO_2 and CaO, followed by Al_2O_3 and MnO (Frias et al., 2006). Figure 8 represents the
409 comparison between the composition of cluster 2D and the previous reported relative composition
410 of several SiMn vitrified slags. Despite O is not included in the SEM-EDX analysis, assuming
411 that chemical speciation of Si, Ca, Al and Mn is in the form of SiO_2, CaO, Al_2O_3 and MnO,

412 respectively, it can be seen from Figure 8 that elemental composition of SiMn slags is in general
413 agreement with the composition of cluster 2D. This is also in accordance with the identification
414 by XRD of alabandite, which has been related to vitrified SiMn slags (Ayala and Fernández,
415 2015). In addition, since several groups of particles with different Si/Al content have also been
416 identified, and taking into account that the uncontrolled cooling of the slag can lead to a different
417 degree of crystallization (Nath et al., 2016), the presence of clusters 4D, 8D or 9D may also be
418 related to SiMn slags. Moreover, as Figure 9 shows, the relative composition of cluster 5D is in
419 accordance with that of a high-Mn FeMn slag reported in a previous study (Rai et al., 2002). The
420 lower abundance of these particles in relation with other clusters attributed to vitrified or partially
421 crystallized SiMn slags (2D and 4D, respectively), may be associated with the reuse of FeMn
422 slags as a Mn source in the SiMn alloy production process, leading to fewer handling steps of the
423 slag and, therefore less fugitive emissions of these particles. It should be noted that up to 70 % of
424 particles detected in deposition and roof dust samples may be attributed to ferromanganese alloys
425 and slags. This is in agreement with the high contribution of the fugitive emissions from metal
426 and slag tapping, casting, crushing and screening to the total Mn emissions in the Mn alloy
427 production (Davourie et al., 2016). According to the literature the Mn solubility from
428 silicomanganese (Thomassen et al., 2001; Ellingsen et al., 2003) and from Mn slags is expected
429 to be very low. Therefore, potential harmful effects of Mn-bearing particles from atmospheric
430 deposition are supposed to be lower with respect to PM_{10}.

431 Additionally, composition and morphology of cluster 3D have been attributed to Mn ores.
432 Several crystallographic phases identified in deposition and roof dust samples, also detected in
433 PM_{10} samples, for instance bixbyite (Mn_2O_3, and $FeMnO_3$), manganese dioxide (MnO_2) and
434 rhodochrosite ($MnCO_3$) (see Table 4) have been previously related to Mn ores (Arndt et al., 2016;
435 Baioumy et al., 2013). Also dolomite has been previously reported in relation with this minerals
436 (He et al., 2016). Other identified phases, such as hausmannite (Mn_3O_4, manganocalcite
437 ($(Ca,Mn)CO_3$) and mangonosite (MnO), previously observed in the wet scrubber sludge (Shen et
438 al., 2005), may be attributed to emissions originated at the Mn ore storage and the ferroalloy
439 milling process. As in PM_{10} samples, some compounds attributed to common raw materials used

440 in the FeMn and SiMn production were identified in deposition and roof dust samples, primarily
441 quartz and calcite, probably related to clusters 6D and 10D.

442 **5. Conclusions**

443 Most of the particles observed by SEM-EDX in PM_{10}, deposition and roof dust samples
444 collected in a residential area in the vicinities of a ferromanganese alloy plant, where Mn air
445 concentrations exceed the WHO guidelines, contain Mn. However, few Mn compounds were
446 detected by XRD in PM_{10} samples probably due to the few amount of particles and the poor
447 crystallinity of the Mn compounds present in this matrix. More Mn phases were detected by XRD
448 in deposition and roof dust samples (e.g. bixbyite, rhodochrosite, manganosite and hausmannite).
449 Around 60% of Mn-PM_{10} particles showed spherical shapes and small sizes and were attributed
450 to condensation processes at the smelting unit of the Mn alloy plant. Due to the neurotoxic effect
451 of Mn and taking into account the shape and small size of these particles, most of them in the
452 submicron range, it is necessary to further investigate their potential toxicity and health effects.

453 Mn-bearing particles were also dominant in the deposition samples, most of them consisting of
454 SiMn slags, Mn alloys and Mn ores, and were mainly attributed to diffuse emissions from raw
455 material and slag/product handling and processing, as well as to diffuse and confined emissions
456 from the smelting building. These particles are characterized by irregular shapes and bigger sizes
457 with respect to PM_{10}, therefore they are expected to be less harmful. In addition, the Mn solubility
458 from Mn slags and alloys is expected to be very low.

459 The application of SEM-EDX and XRD to the characterization of PM_{10}, deposition and roof
460 dust samples has been crucial to better understand the significant differences in the
461 physicochemical characteristics of the Mn-bearing particles sourcing from a ferromanganese
462 alloy plant. The main results derived from this characterization indicate that Mn occurs in various
463 oxidation states, some of them highly soluble, and is mainly associated with submicronic particles
464 known to be the most harmful for health. Thus, Mn contained in spherical small particles is
465 expected to be much more bioaccessible than that found in coarser particles detected in deposition

466 samples. Therefore, the use of these techniques can be a valuable tool, leading to an improvement
467 in the assessment of Mn potential hazardous effects on human health.

468 **Acknowledgements**

469 This work has been financially supported by the Spanish Ministry of Economy and
470 Competitiveness (MINECO) through the Project CTM2013-43904R. Ana Hernández-Pellón
471 thanks the Ministry of Economy and Competitiveness (MINECO) for the FPI grant awarded,
472 BES-2014-068790.

473

474

475 **References**

476 Agency for Toxic Substances and Disease Registry (ATSDR), 2012. U.S. Department of health
477 and human services, Public Health Service. Toxicological profile for manganese.

478 Ali-Khodja H, Belaala A, Demmane-DebbihW, Habbas B, B., N, 2008. Air quality and deposition
479 of trace elements in Dodouche Mourad, Algeria. Env. Monit Assess 138, 219–231.

480 Arndt, J., Deboudt, K., Anderson, A., Blondel, A., Eliet, S., Flament, P., Fourmentin, M., Healy,
481 R.M., Savary, V., Setyan, A., Wenger, J.C., 2016. Scanning electron microscopy-energy
482 dispersive X-ray spectrometry (SEM-EDX) and aerosol time-of-flight mass spectrometry
483 (ATOFMS) single particle analysis of metallurgy plant emissions. Environ. Pollut. 210, 9–17.
484 doi:10.1016/j.envpol.2015.11.019

485 Arruti, A., Fernández-Olmo, I., Irabien, A., 2010. Evaluation of the contribution of local sources
486 to trace metals levels in urban PM2.5 and PM10 in the Cantabria region (Northern Spain). J.
487 Environ. Monit. 12, 1451–1458. doi:10.1039/b926740a

488 Ayala, J., Fernández, B., 2015. Recovery of manganese from silicomanganese slag by means of
489 a hydrometallurgical process. Hydrometallurgy 158, 68–73. doi:10.1016/j.hydromet.2015.10.007

Baioumy, H.M., Khedr, M.Z., Ahmed, A.H., 2013. Mineralogy, geochemistry and origin of Mn in the high-Mn iron ores, Bahariya Oasis, Egypt. Ore Geol. Rev. 53, 63–76. doi:10.1016/j.oregeorev.2012.12.009

Bondarenko, I., Treiger, B., Van Grieken, R., Van Espen, P., 1996. IDAS: A Windows based software package for cluster analysis. Spectrochim. Acta - Part B At. Spectrosc. 51, 441–456. doi:10.1016/0584-8547(95)01448-9

Boudissa, S.M., Lambert, J., Müller, C., Kennedy, G., Gareau, L., Zayed, J., 2006. Manganese concentrations in the soil and air in the vicinity of a closed manganese alloy production plant. Sci. Total Environ. 361, 67–72. doi:10.1016/j.scitotenv.2005.05.001

Cantabria, C.G. of, 2006. Evaluation of the influence of wind direction on manganese content of PM10 collected in Alto de Maliaño.

Carvalho, C.F., Menezes-Filho, J.A., Matos, V.P. de, Bessa, J.R., Coelho-Santos, J., Viana, G.F.S., Argollo, N., Abreu, N., 2014. Elevated airborne manganese and low executive function in school-aged children in Brazil. Neurotoxicology 45, 301–308. doi:10.1016/j.neuro.2013.11.006

Castillo, S., De la Rosa, J.D., Sánchez de la Campa, A.M., González-Castanedo, Y., Fernández-Camacho, R., 2013. Heavy metal deposition fluxes affecting an Atlantic coastal area in the southwest of Spain. Atmos. Environ. 77, 509–517. doi:10.1016/j.atmosenv.2013.05.046

Chattopadhyay, G., Lin, K.C.P., Feitz, A.J., 2003. Household dust metal levels in the Sydney metropolitan area. Environ. Res. 93, 301–307. doi:10.1016/S0013-9351(03)00058-6

Chen, P., Culbreth, M., Aschner, M., 2016. Exposure, epidemiology, and mechanism of the environmental toxicant manganese. Environ. Sci. Pollut. Res. 23, 13802–13810. doi:10.1007/s11356-016-6687-0

CIMA, Government of Cantabria, 2010. Evaluación de la calidad del aire y analítica de metales en la fracción PM10 en el Alto Maliaño. Internal Report C-077/2008.

515 CIMA. Government of Cantabria, 2006. Evaluation of the influence of wind direction on
516 manganese content of PM10 collected in Alto Maliaño. Internal Report C-098/2004.4.

517 Crossgrove, J., Zheng, W., 2004. Manganese toxicity upon overexposure. NMR Biomed. 17, 544–
518 553. doi:10.1002/nbm.931

519 Davourie, J., Westfall, L., Ali, M., McGough, D., 2016. Evaluation of particulate matter emissions
520 from manganese alloy production using life-cycle assessment. Neurotoxicology 3. In press
521 doi:http://dx.doi.org/10.1016/j.neuro.2016.09.015

522 Dieme, D., Cabral-Ndior, M., Garçon, G., Verdin, A., Billet, S., Cazier, F., Courcot, D., Diouf,
523 A., Shirali, P., 2012. Relationship between physicochemical characterization and toxicity of fine
524 particulate matter (PM 2.5) collected in Dakar city (Senegal). Environ. Res. 113, 1–13.
525 doi:10.1016/j.envres.2011.11.009

526 Elder, A., Gelein, R., Silva, V., Feikert, T., Opanashuk, L., Carter, J., Potter, R., Maynard, A., Ito,
527 Y., Finkelstein, J., Oberdörster, G., 2006. Translocation of inhaled ultrafine manganese oxide
528 particles to the central nervous system. Environ. Health Perspect. 114, 1172–1178.
529 doi:10.1289/ehp.9030

530 Ellingsen, D.G., Hetland, S.M., Thomassen, Y., 2003. Manganese air exposure assessment and
531 biological monitoring in the manganese alloy production industry. J. Environ. Monit. 5, 84–90.
532 doi:10.1039/b209095c

533 Ellingsen, D.G., Zibarev, E., Kusraeva, Z., Berlinger, B., Chashchin, M., Bast-Pettersen, R.,
534 Chashchin, V. and Thomassen Y., 2013. The bioavailability of manganese in welders in relation
535 to its solubility in welding fumes. Environ Sci Process Impacts, 15(2):357-365.Fernández-Olmo,
536 I., Puente, M., Irabien, A., 2015. A comparative study between the fluxes of trace elements in
537 atmospheric deposition at industrial, urban, traffic, and rural sites. Environ. Sci. Pollut. Res. 22,
538 13427–13441. doi:10.1007/s11356-015-4562-z

539 Ferroatlántica S.L., 2013. Declaración ambiental. División Electrometalurgia. Centro productivo:
540 Fábrica de Boo.

541 Flynn, M.R., Susi, P., 2009. Neurological risks associated with manganese exposure from welding
542 operations - A literature review. Int. J. Hyg. Environ. Health 212, 459–469.
543 doi:10.1016/j.ijheh.2008.12.003

544 Freeland-Graves, J.H., Mousa, T.Y., Sanjeevi, N., 2015. Nutritional requirements for manganese,
545 Issues in Toxicology, 22, 34-75.

546 Frias, M., Sánchez De Rojas, M.I., Santamaría, J., Rodríguez, C., 2006. Recycling of
547 silicomanganese slag as pozzolanic material in Portland cements: Basic and engineering
548 properties. Cem. Concr. Res. 36, 487–491. doi:10.1016/j.cemconres.2005.06.014

549 Gjønnes, K., Skogstad, A., Hetland, S., Ellingsen, D.G., Thomassen, Y., Weinbruch, S., 2011.
550 Characterisation of workplace aerosols in the manganese alloy production industry by electron
551 microscopy. Anal. Bioanal. Chem. 399, 1011–1020. doi:10.1007/s00216-010-4470-5

552 González, L.T., Rodríguez, F.E.L., Sánchez-Domínguez, M., Leyva-Porras, C., Silva-Vidaurri,
553 L.G., Acuna-Askar, K., Kharisov, B.I., Villarreal Chiu, J.F., Alfaro Barbosa, J.M., 2016.
554 Chemical and morphological characterization of TSP and PM2.5 by SEM-EDS, XPS and XRD
555 collected in the metropolitan area of Monterrey, Mexico. Atmospheric Environment 143, 249-
556 260. doi:10.1016/j.atmosenv.2016.08.053

557 Gunst, S., Weinbruch, S., Wentzel, M., Ortner, H.M., Skogstad, A., Hetland, S., Thomassen, Y.,
558 2000. Chemical composition of individual aerosol particles in workplace air during production of
559 manganese alloys. J. Environ. Monit. 2, 65–71. doi:10.1039/a908329d

560 Haynes, E.N., Heckel, P., Ryan, P., Roda, S., Leung, Y.K., Sebastian, K., Succop, P., 2010.
561 Environmental manganese exposure in residents living near a ferromanganese refinery in
562 Southeast Ohio: A pilot study. Neurotoxicology 31, 468–474. doi:10.1016/j.neuro.2009.10.011

He, H., Cao, J., Duan, N., 2016. Analytical and mineralogical study of a Ghana manganese ore: Quantification of Mn speciation and effect of mechanical activation. Chemosphere 162, 8–15. doi:10.1016/j.chemosphere.2016.07.061

Hernández-Pellón A., Fernández-Olmo, I., 2016. Monitoring the levels of particle matter-bound manganese: An intensive campaign in an urban/industrial area. II International Conference on Atmospheric Dust (DUST 2016). Scientific Research Abstracts 5, 7.

Keen, C.L., Ensunsa, J.L., Clegg, M.S., 2000. Manganese metabolism in animals and humans including the toxicity of manganese. Met. Ions Biol. Syst. 37, 89-121.

Kero, I., Naess, M.K., Tranell, G., 2015. Particle Size Distributions of Particulate Emissions from the Ferroalloy Industry Evaluated by Electrical Low Pressure Impactor (ELPI). J. Occup. Environ. Hyg. 9624, 37–44. doi:10.1080/15459624.2014.935783

Kwakye, G.F., Paoliello, M.M.B., Mukhopadhyay, S., Bowman, A.B., Aschner, M., 2015. Manganese-induced parkinsonism and Parkinson's disease: Shared and distinguishable features. Int. J. Environ. Res. Public Health 12(7), 7519-7540 doi:10.3390/ijerph120707519

Ledoux, F., Laversin, H., Courcot, D., Courcot, L., Zhilinskaya, E.A., Puskaric, E., Aboukaïs, A., 2006. Characterization of iron and manganese species in atmospheric aerosols from anthropogenic sources. Atmos. Res. 82, 622–632. doi:10.1016/j.atmosres.2006.02.018

Lucchini, R.G., Guazzetti, S., Zoni, S., Donna, F., Peter, S., Zacco, A., Salmistraro, M., Bontempi, E., Zimmerman, N.J., Smith, D.R., 2012. Tremor, olfactory and motor changes in Italian adolescents exposed to historical ferro-manganese emission. Neurotoxicology 33, 687–696. doi:10.1016/j.neuro.2012.01.005

Majestic, B. J., Schauer, J. J. and Shafer, M. M., 2007. Development of a manganese speciation method for atmospheric aerosols in biologically and environmentally relevant fluids. Aerosol Science and Technology 41(10), 925-933. doi:10.1080/02786820701564657

587 Marris, H., Deboudt, K., Augustin, P., Flament, P., Blond, F., Fiani, E., Fourmentin, M., Delbarre,
588 H., 2012. Fast changes in chemical composition and size distribution of fine particles during the
589 near-field transport of industrial plumes. Sci. Total Environ. 427–428, 126–138.
590 doi:10.1016/j.scitotenv.2012.03.068

591 Marris, H., Deboudt, K., Flament, P., Grobéty, B., Gieré, R., 2013. Fe and Mn oxidation states by
592 TEM-EELS in fine-particle emissions from a Fe-Mn alloy making plant. Environ. Sci. Technol.
593 47, 10832–10840. doi:10.1021/es400368s

594 Megido, L., Suárez-Peñaa, B., Negral, L., Castrillón, L., Suárez, S., Fernández-Nava, Y.,
595 Marañón, E., 2016. Relationship between physico-chemical characteristics and potential toxicity
596 of PM10. Chemosphere 162, 73–79. doi:10.1016/j.chemosphere.2016.07.067

597 Menezes-Filho, J.A., Novaes, C. de O., Moreira, J.C., Sarcinelli, P.N., Mergler, D., 2011.
598 Elevated manganese and cognitive performance in school-aged children and their mothers.
599 Environ. Res. 111, 156–163. doi:10.1016/j.envres.2010.09.006

600 Mijić, Z., Stojić, A., Perišić, M., Rajšić, S., Tasić, M., Radenković, M., Joksić, J., 2010. Seasonal
601 variability and source apportionment of metals in the atmospheric deposition in Belgrade. Atmos.
602 Environ. 44, 3630–3637. doi:10.1016/j.atmosenv.2010.06.045

603 Moreno, T., Pandolfi, M., Querol, X., Lavín, J., Alastuey, A., Viana, M., Gibbons, W., 2011.
604 Manganese in the urban atmosphere: Identifying anomalous concentrations and sources. Environ.
605 Sci. Pollut. Res. 18, 173–183. doi:10.1007/s11356-010-0353-8

606 Nath, S.K., Kumar, S., 2016. Evaluation of the suitability of ground granulated silico-manganese
607 slag in Portland slag cement. Constr. Build. Mater. 125, 127–134.
608 doi:10.1016/j.conbuildmat.2016.08.025Park, R.M., 2013. Neurobehavioral deficits and
609 parkinsonism in occupations with manganese exposure: A review of methodological issues in the
610 epidemiological literature. Saf. Health Work 4(3), 123-135. doi:10.1016/j.shaw.2013.07.003

611 Pavilonis, B.T., Lioy, P.J., Guazzetti, S., Bostick, B.C., Donna, F., Peli, M., Zimmerman, N.J.,
612 Bertrand, P., Lucas, E., Smith, D.R., Georgopoulos, P.G., Mi, Z., Royce, S.G., Lucchini, R.G.,
613 2015. Manganese concentrations in soil and settled dust in an area with historic ferroalloy
614 production. J. Expo. Sci. Environ. Epidemiol. 25, 443–450. doi:10.1038/jes.2014.70

615 Perrone, M.G., Gualtieri, M., Ferrero, L., Porto, C. Lo, Udisti, R., Bolzacchini, E., Camatini, M.,
616 2010. Seasonal variations in chemical composition and in vitro biological effects of fine PM from
617 Milan. Chemosphere 78, 1368–1377. doi:10.1016/j.chemosphere.2009.12.071

618 Qin, J., Nworie, O.E., Lin, C., 2016. Particle size effects on bioaccessible amounts of ingestible
619 soil-borne toxic elements. Chemosphere 159, 442–448. doi:10.1016/j.chemosphere.2016.06.034

620 Querol, X., Viana, M., Alastuey, A., Amato, F., Moreno, T., Castillo, S., Pey, J., de la Rosa, J.,
621 Sánchez de la Campa, A., Artíñano, B., Salvador, P., García Dos Santos, S., Fernández-Patier, R.,
622 Moreno-Grau, S., Negral, L., Minguillón, M.C., Monfort, E., Gil, J.I., Inza, A., Ortega, L.A.,
623 Santamaría, J.M., Zabalza, J., 2007. Source origin of trace elements in PM from regional
624 background, urban and industrial sites of Spain. Atmos. Environ. 41, 7219–7231.
625 doi:10.1016/j.atmosenv.2007.05.022

626 Rai, A., Prabakar, J., Raju, C.B., Morchalle, R.K., 2002. Metallurgical slag as a component in
627 blended cement. Constr. Build. Mater. 16, 489–494. doi:10.1016/S0950-0618(02)00046-6

628 Riojas-Rodríguez, H., Solís-Vivanco, R., Schilmann, A., Montes, S., Rodríguez, S., Ríos, C.,
629 Rodríguez-Agudelo, Y., 2010. Intellectual function in Mexican children living in a mining area
630 and environmentally exposed to manganese. Environ. Health Perspect. 118, 1465–1470.
631 doi:10.1289/ehp.0901229

632 Rodríguez-Agudelo, Y., Riojas-Rodríguez, H., Ríos, C., Rosas, I., Sabido Pedraza, E., Miranda,
633 J., Siebe, C., Texcalac, J.L., Santos-Burgoa, C., 2006. Motor alterations associated with exposure
634 to manganese in the environment in Mexico. Sci. Total Environ. 368, 542–556.
635 doi:10.1016/j.scitotenv.2006.03.025

636 Rodríguez-Barranco, M., Lacasaña, M., Aguilar-Garduño, C., Alguacil, J., Gil, F., González-
637 Alzaga, B., Rojas-García, A., 2013. Association of arsenic, cadmium and manganese exposure
638 with neurodevelopment and behavioural disorders in children: A systematic review and meta-
639 analysis. Sci. Total Environ. 454–455, 562–577. doi:10.1016/j.scitotenv.2013.03.047

640 Roels, H.A., Bowler, R.M., Kim, Y., Claus Henn, B., Mergler, D., Hoet, P., Gocheva, V. V.,
641 Bellinger, D.C., Wright, R.O., Harris, M.G., Chang, Y., Bouchard, M.F., Riojas-Rodriguez, H.,
642 Menezes-Filho, J.A., Téllez-Rojo, M.M., 2012. Manganese exposure and cognitive deficits: A
643 growing concern for manganese neurotoxicity. Neurotoxicology 33, 872–880.
644 doi:10.1016/j.neuro.2012.03.009

645 Rosas Pérez, I., Serrano, J., Alfaro-Moreno, E., Baumgardner, D., García-Cuellar, C., Martín del
646 Campo, J.M., Raga, G.B., Castillejos, M., Colín, R.D., Osornio Vargas, A.R., 2007. Relations
647 between PM10 composition and cell toxicity: A multivariate and graphical approach.
648 Chemosphere 67, 1218–1228. doi:10.1016/j.chemosphere.2006.10.078

649 Rossini, P., Matteucci, G., Guerzoni, S., 2010. Atmospheric fall-out of metals around the Murano
650 glass-making district (Venice, Italy). Environ. Sci. Pollut. Res. 17, 40–48. doi:10.1007/s11356-
651 009-0122-8

652 Ruiz, S., Fernández-Olmo, I., Irabien, Ángel, 2014. Discussion on graphical methods to identify
653 point sources from wind and particulate matter-bound metal data. Urban Clim. 10, 671–681.
654 doi:10.1016/j.uclim.2013.11.001

655 Santamaria, A.B., 2008. Manganese exposure, essentiality & toxicity. Indian J. Med. Res. 128,
656 484–500. doi:10.5897/AJEST12.196

657 Shen, R., Zhang, G., Dell'Amico, M., Brown, P., Ostrovski, O., 2005. Characterisation of
658 Manganese Furnace Dust and Zinc Balance in Production of Manganese Alloys. ISIJ Int. 45,
659 1248–1254. doi:10.2355/isijinternational.45.1248

660 Sturges, W.T., Harrison, R.M., 1989. Semi-quantitative x-ray diffraction analysis of size
661 fractionated atmospheric particles. Atmospheric Environment (1967) 23, 1083-1098.
662 doi:10.1016/0004-6981(89)90309

663 Sunyer, J., 2008. The neurological effects of air pollution in children. Eur. Respir. J. 32, 535–537.
664 doi:10.1183/09031936.00073708Thomassen, Y., Ellingsen, D.G., Hetland, S., Sand, G., 2001.
665 Chemical speciation and sequential extraction of Mn in workroom aerosols: analytical
666 methodology and results from a field study in Mn alloy plants. J. Environ. Monit. 3, 555–559.
667 doi:10.1039/b104479f

668 WHO, 2000. Air quality guidelines for Europe. WHO Regional Publications, European Series,
669 No. 91.

670 Žibret, G., Rokavec, D., 2010. Household dust and street sediment as an indicator of recent heavy
671 metals in atmospheric emissions: A case study on a previously heavily contaminated area.
672 Environ. Earth Sci. 61, 443–453. doi:10.1007/s12665-009-0356-2

Figure Captions

Figure 1: Flow diagram of a ferromanganese alloy plant showing the point and fugitive sources of PM. The diagram shows the sites where samples have been collected and physico-chemically characterized according to the literature (stacks, filters and sludges, indoor air, outdoor air)

Figure 2: Sampling points and manganese sources

Figure 3: SEM images (secondary electrons) of particles in PM_{10} samples collected at CCV site (labels correspond to cluster number as given in Table 2)

Figure 4: SEM images (back-scattered electrons) of particles in deposition samples collected at CCV site (labels correspond to cluster number and indicate the type of particle as defined in Table 3)

Figure 5: X-ray diffractograms of PM_{10} collected at CROS site. Peak labels: Gy: gypsum; Q: quartz; Ca: calcite; Rh: rhodochrosite; M: manganese dioxide; A: aluminum silicate; B: bixbyite

Figure 6: X-ray diffractograms of Deposition (Dep) and Roof Dust (RD) collected at CCV site. Peak labels: Gy: gypsum; Q: quartz; Ca: calcite; D: dolomite; Rh: rhodochrosite; Bi: bixbyite; Mi: Manganese iron silicon; Ma: manganocalcite; Bu: bustamite; Mc: microcline; Ha: hausmannite; S: alabandite; Mo: manganosite or iron manganese oxide; H: hematite; F: magnetite; Si: silicates.

Figure 7: Comparison between relative elemental composition of cluster 1D and the weighted annual average composition of FeMn HC, FeMn MC and SiMn.

Figure 8: Comparison between relative elemental composition of cluster 2D and several SiMn slags.

Figure 9: Comparison between relative elemental composition of cluster 4D and a high-Mn FeMn slag.

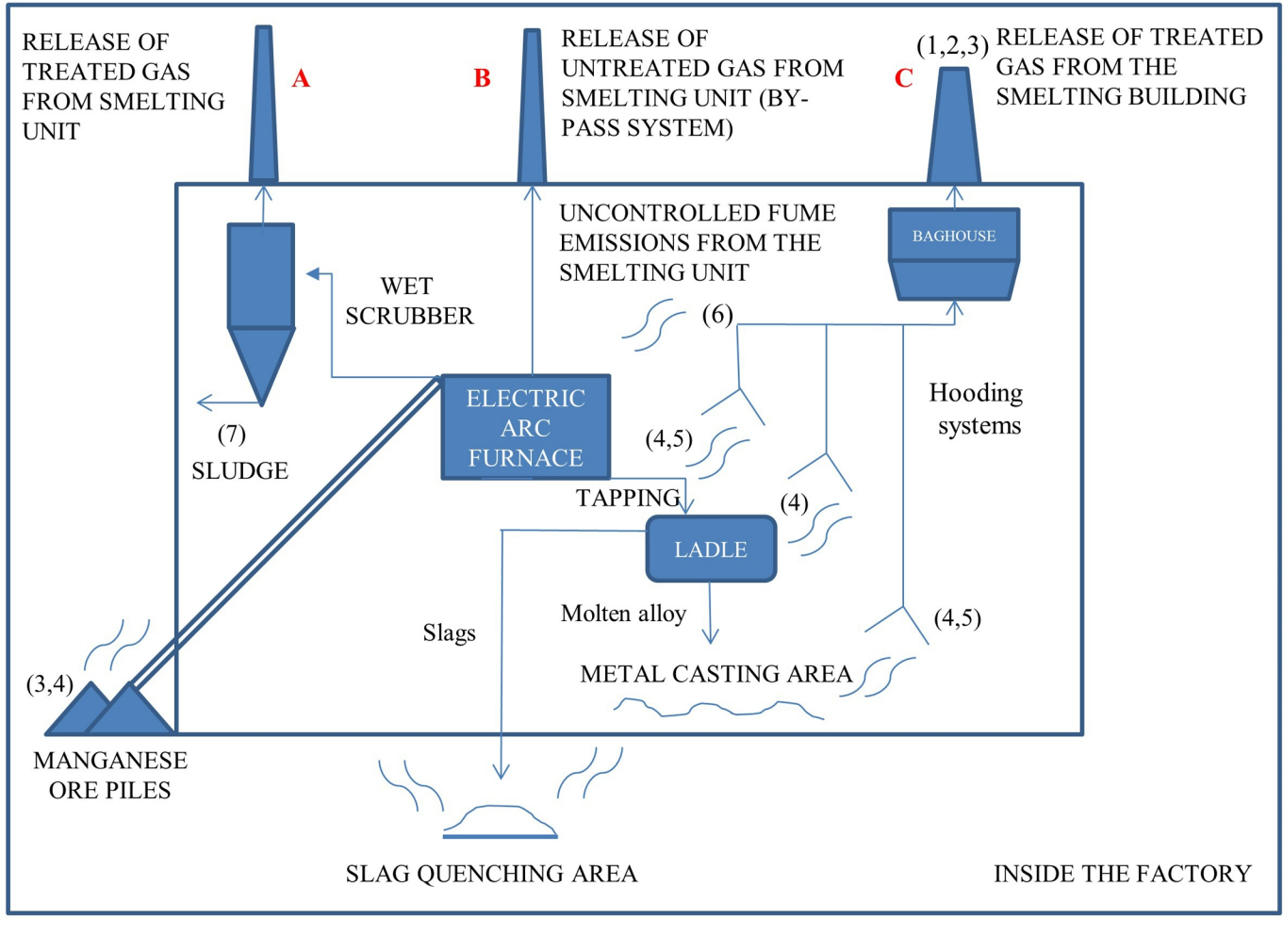
RELEASE OF TREATED GAS FROM SMELTING UNIT
A
B
RELEASE OF UNTREATED GAS FROM SMELTING UNIT (BY-PASS SYSTEM)
(1,2,3)
C
RELEASE OF TREATED GAS FROM THE SMELTING BUILDING
UNCONTROLLED FUME EMISSIONS FROM THE SMELTING UNIT
BAGHOUSE
WET SCRUBBER
(6)
Hooding systems
(7)
SLUDGE
ELECTRIC ARC FURNACE
(4,5)
TAPPING
(4)
LADLE
Molten alloy
(4,5)
Slags
METAL CASTING AREA
(3,4)
MANGANESE ORE PILES
SLAG QUENCHING AREA
INSIDE THE FACTORY
OUTSIDE THE FACTORY (1,2,8)

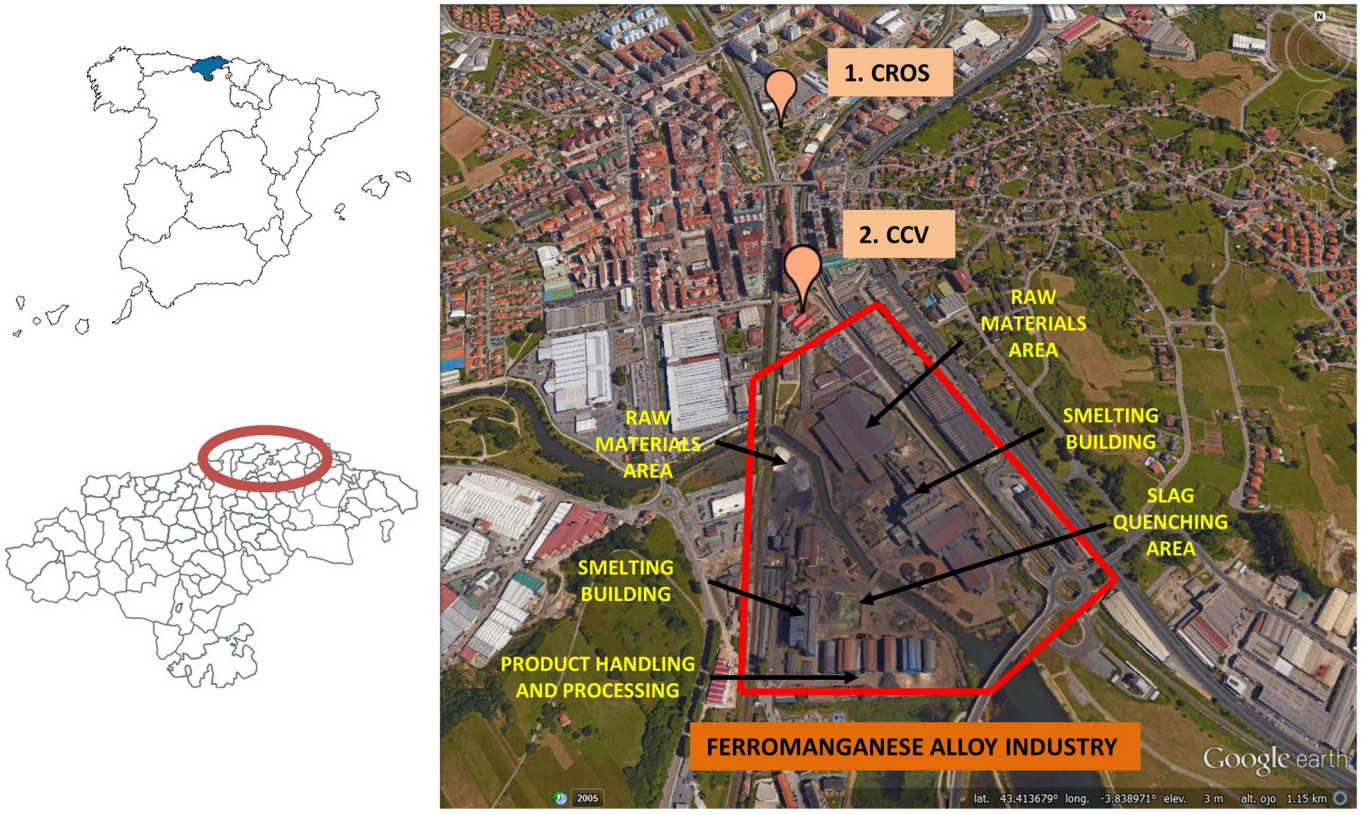
1. CROS
2. CCV
RAW MATERIALS AREA
SMELTING BUILDING
SLAG QUENCHING AREA
RAW MATERIALS AREA
SMELTING BUILDING
PRODUCT HANDLING AND PROCESSING
FERROMANGANESE ALLOY INDUSTRY
Google earth
2005
lat. 43.413679° long. -3.838971° elev. 3 m alt. ojo 1.15 km

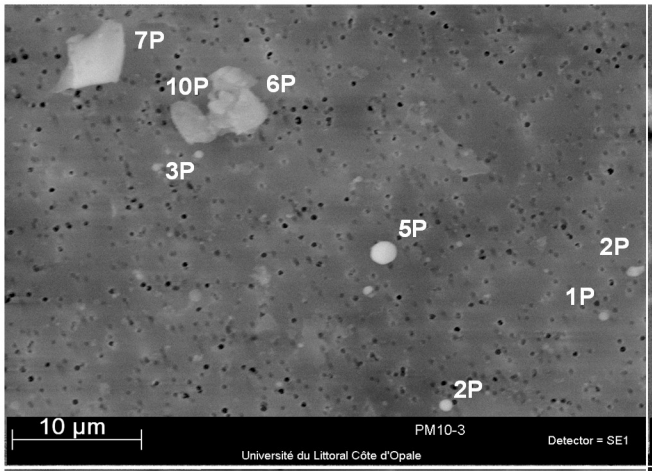
7P
10P
6P
3P
5P
2P
1P
2P
10 µm
PM10-3
Université du Littoral Côte d'Opale
Detector = SE1

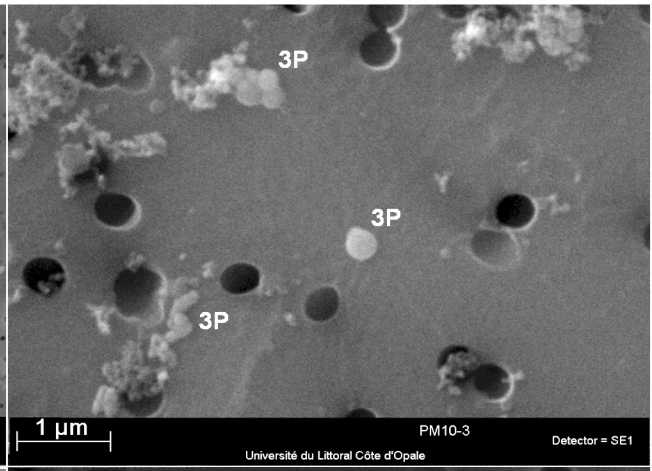
3P
3P
3P
1 µm
PM10-3
Université du Littoral Côte d'Opale
Detector = SE1

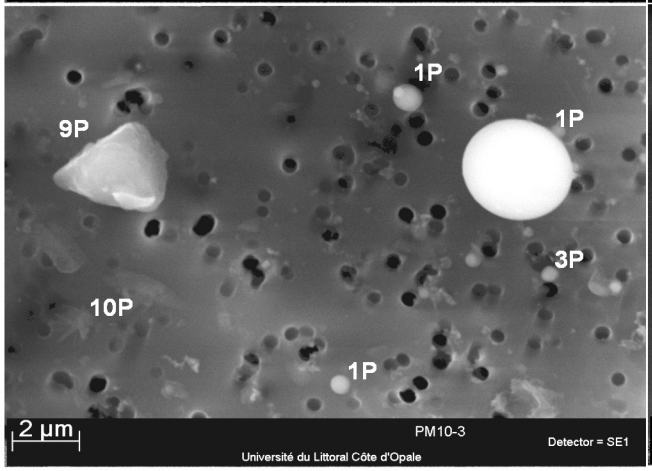
1P
9P
1P
3P
10P
1P
2 µm
PM10-3
Université du Littoral Côte d'Opale
Detector = SE1

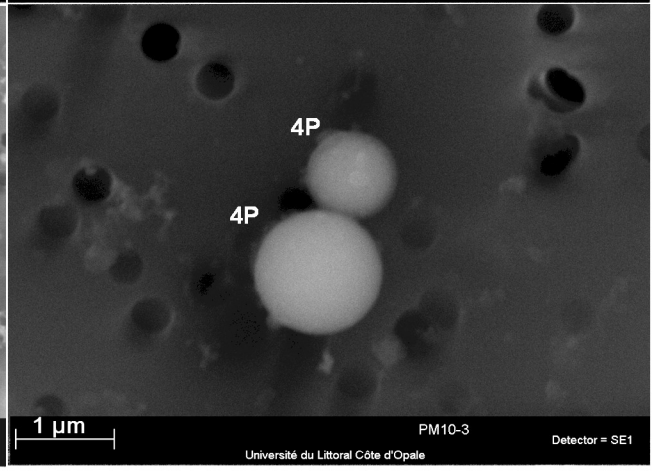
4P
4P
1 µm
PM10-3
Université du Littoral Côte d'Opale
Detector = SE1

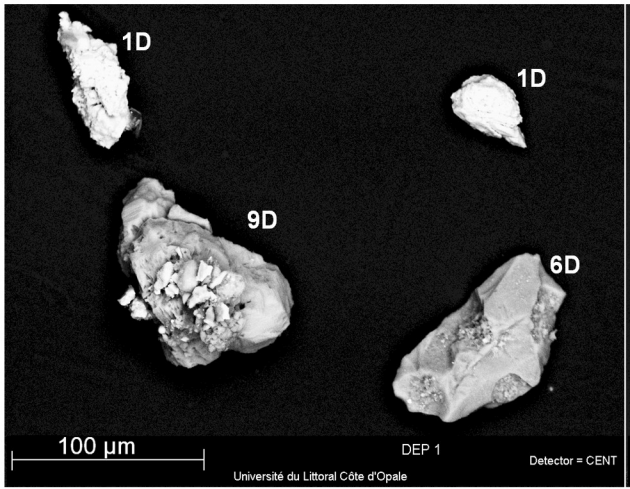
1D
1D
9D
6D
100 µm
DEP 1
Detector = CENT
Université du Littoral Côte d'Opale

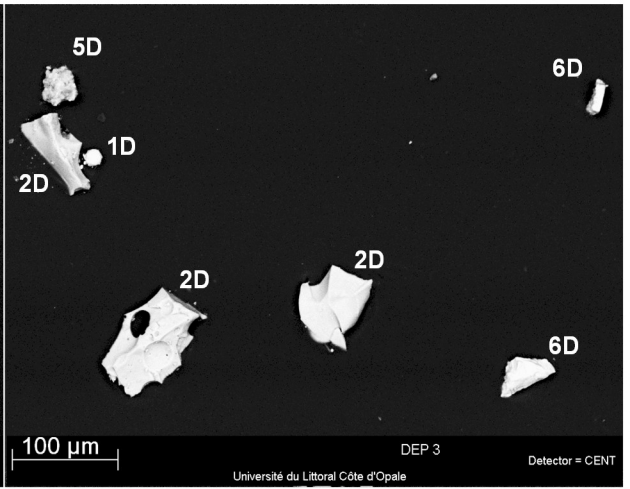
5D
6D
1D
2D
2D
2D
6D
100 µm
DEP 3
Detector = CENT
Université du Littoral Côte d'Opale

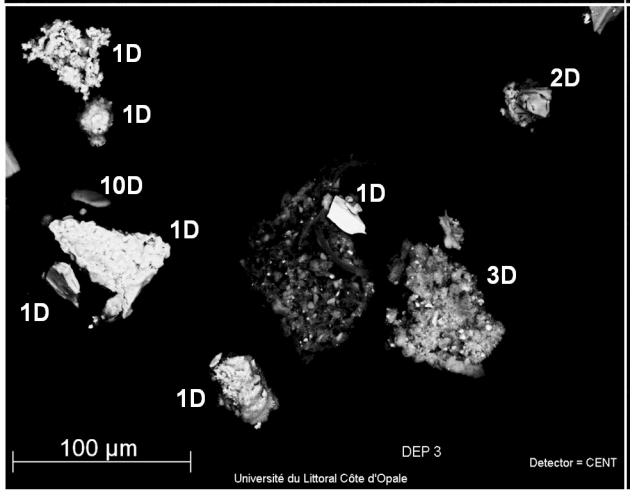
1D
2D
1D
10D
1D
1D
1D
3D
1D
100 µm
DEP 3
Detector = CENT
Université du Littoral Côte d'Opale

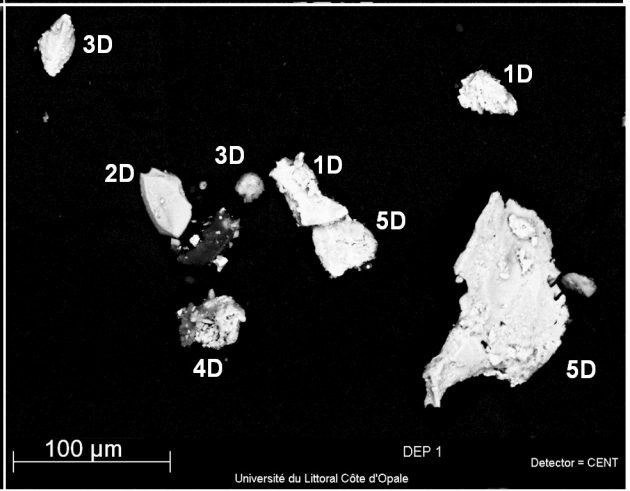
3D
1D
2D
3D
1D
5D
4D
5D
100 µm
DEP 1
Detector = CENT
Université du Littoral Côte d'Opale

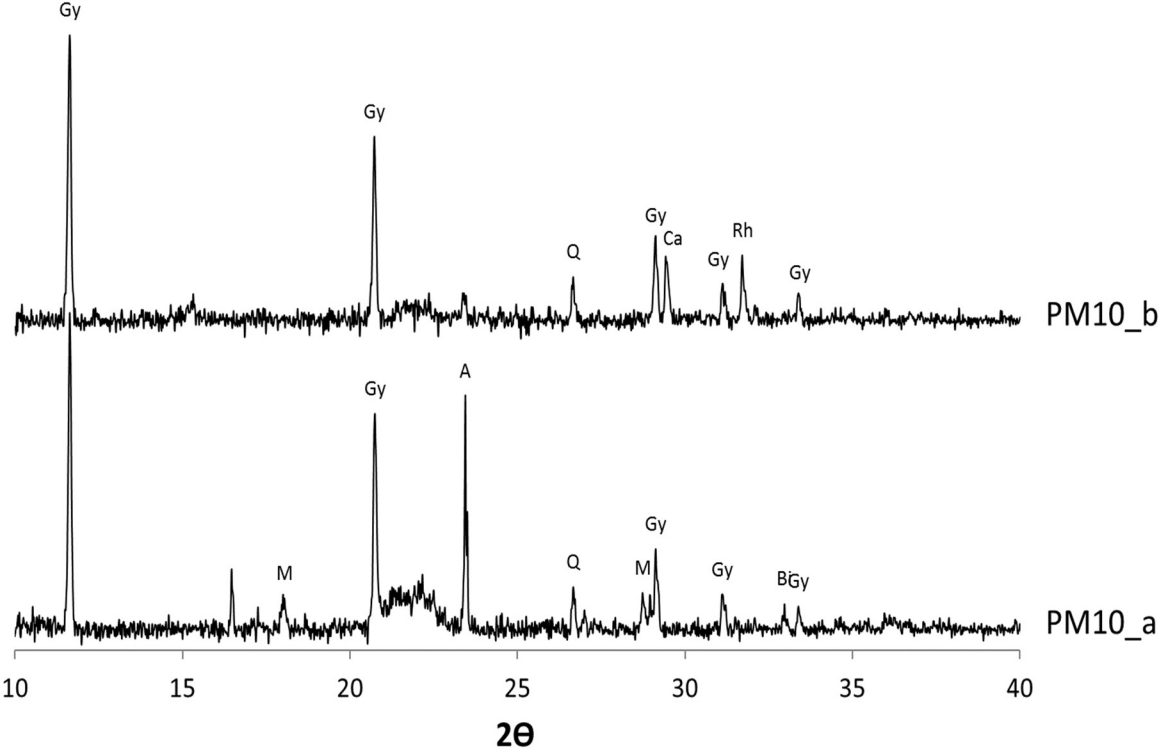
Gy
Gy
Q
Gy
Ca
Gy
Rh
Gy
PM10_b
Gy
A
M
Q
M
Gy
Gy
Gy
PM10_a
10
15
20
25
30
35
40
2Θ

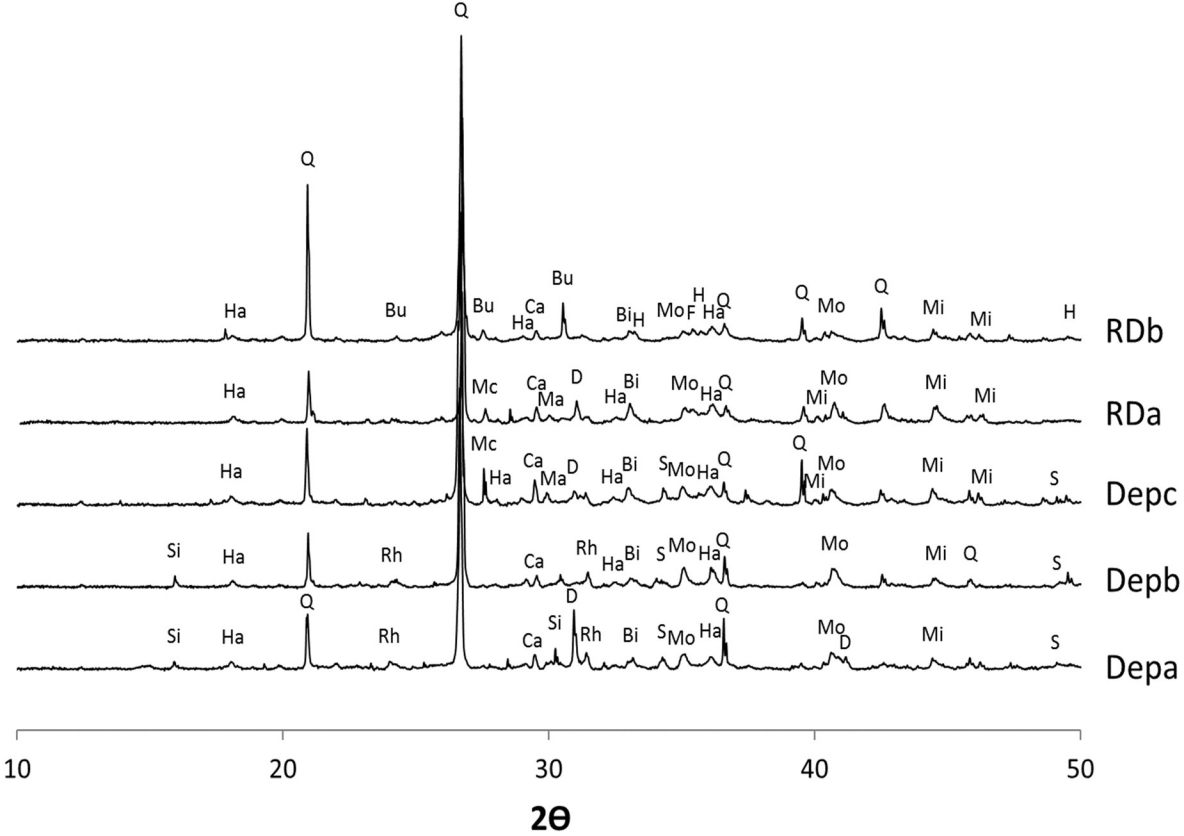
RDb
RDa
Depc
Depb
Depa
2Θ
10
20
30
40
50

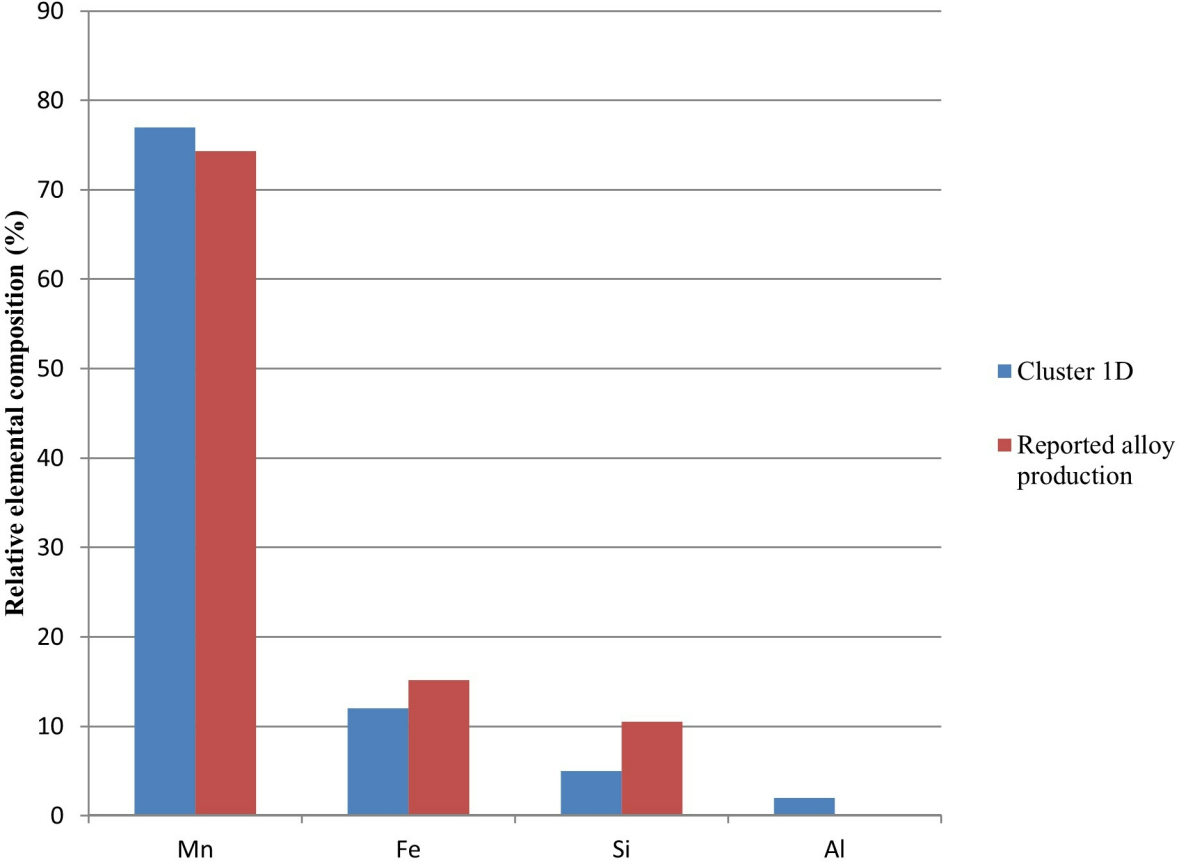
90
80
70
60
50
40
30
20
10
0
Relative elemental composition (%)
Mn
Fe
Si
Al
Cluster 1D
Reported alloy production

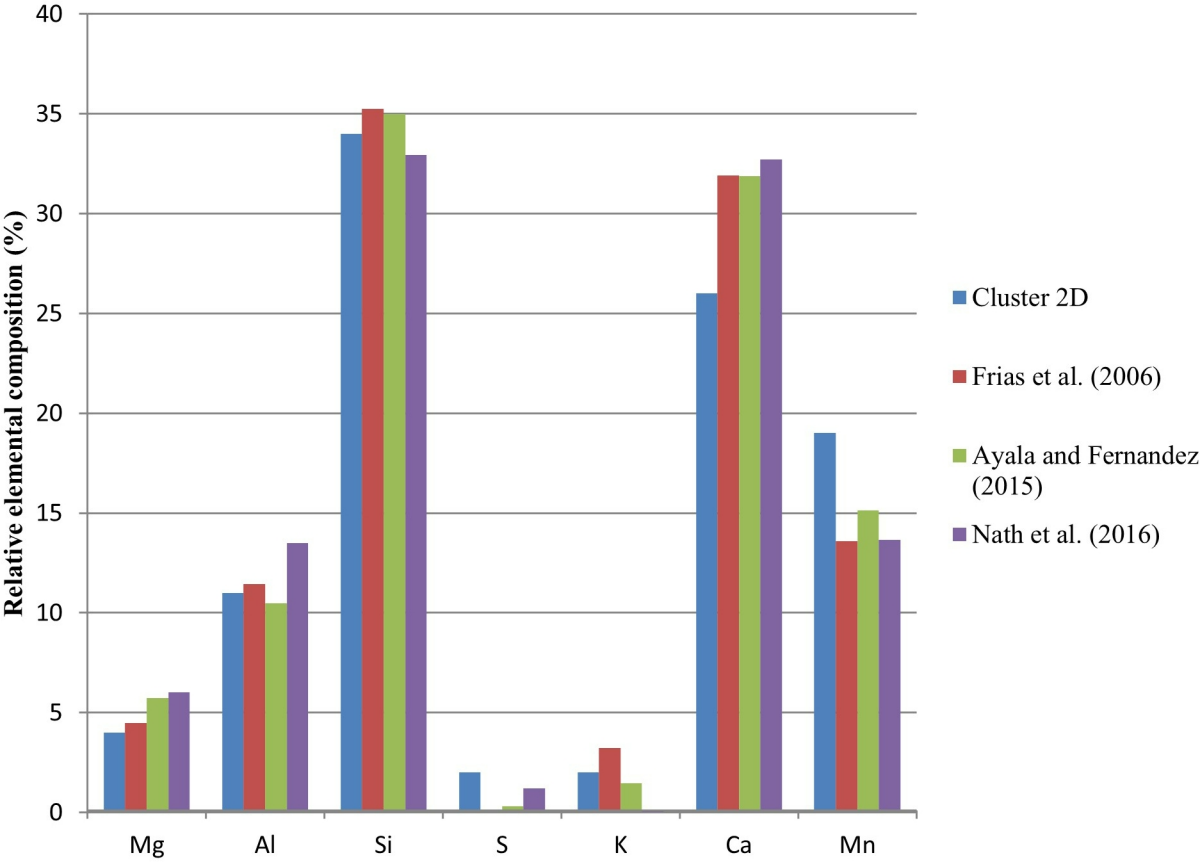
Relative elemental composition (%)
40
35
30
25
20
15
10
5
0
Mg
Al
Si
S
K
Ca
Mn
Cluster 2D
Frias et al. (2006)
Ayala and Fernandez (2015)
Nath et al. (2016)

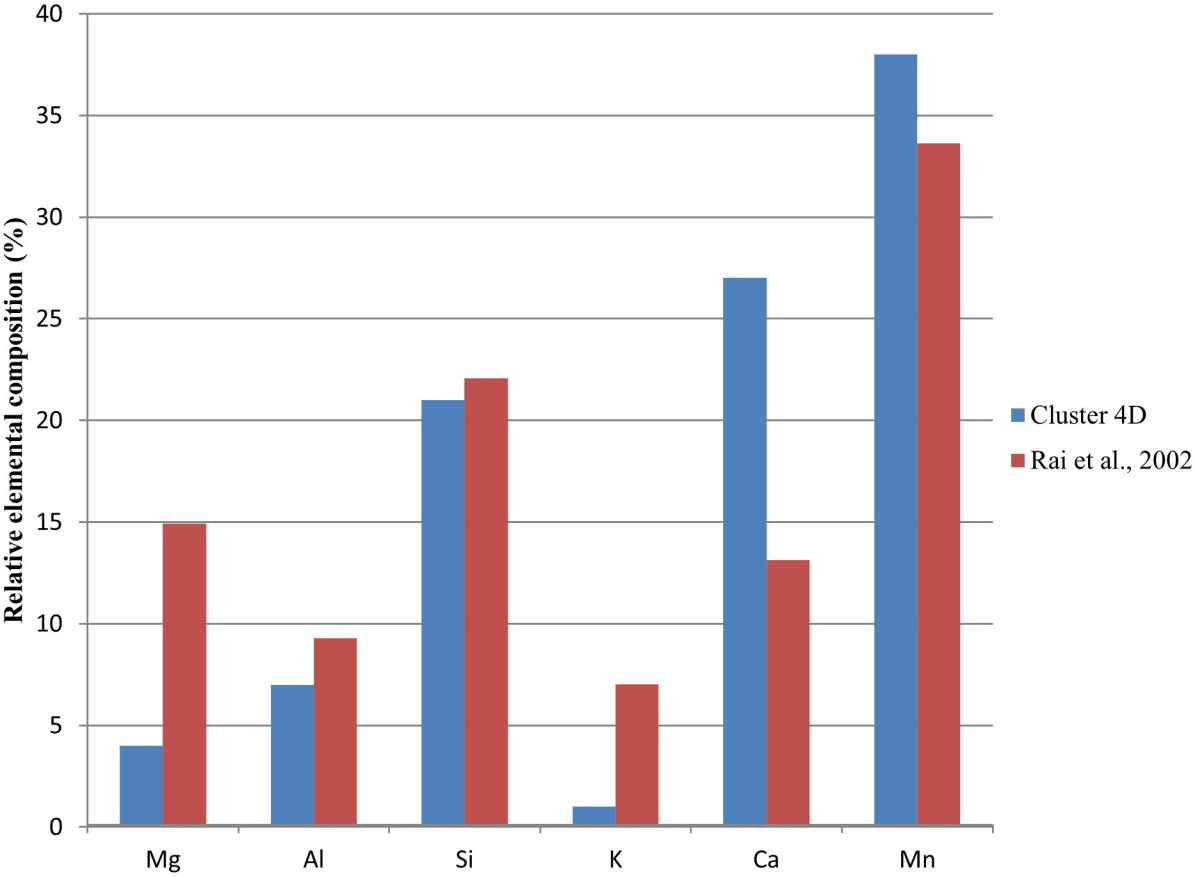
40
35
30
25
20
15
10
5
0
Relative elemental composition (%)
Mg
Al
Si
K
Ca
Mn
Cluster 4D
Rai et al., 2002

Table 1: Mean values and standard deviation (SD) of Mn and Fe, and Mn/Fe ratio in PM_{10}, insoluble fraction of the atmospheric deposition and roof dust samples (RD)

Metal	PM_{10} (ng/m^3)				Atmospheric deposition ($\mu g/m^2 \cdot day$)		Roof dust (RD) <70 μm (mg/kg)		Roof dust (RD) 70-100 μm (mg/kg)	
	CROS site[a]		CCV site[b]		CCV site[c]		CCV site[d]		CCV site[d]	
	Mean	SD	Mean	SD	Mean	SD	Mean	SD	Mean	SD
Mn	231.7	308.7	670.4	652.0	11,355	2,912	322,507	139,275	161,537	211,227
Fe	279.4	225.5	322.0	192.8	5,316	1,468	159,859	44,523	199,517	191,662
Mn/Fe	0.83		2.24		2.14		2.02		0.81	

a Sampling period: January 2015-January-2016 (1 sample per week, a total of 52 samples)
b Sampling period: September 2016 (28 daily samples)
c Sampling period: 2015-2016. Monthly mean values (6 samples). Values correspond to the insoluble fraction of the atmospheric deposition.
d Average value of two samples.

Table 2: Types of particles evidenced in PM_{10} collected at CCV site using SEM-EDX after Hierarchical Cluster Analysis of a dataset containing the individual composition of 1000 particles and corresponding mean diameter (% in brackets corresponds to relative mass composition; elements with Z<=8 were not considered).

Cluster	Relative Abundance (%)	Mean Diameter (μm)	Composition							
1P	21.9	0.67		Si(43)		K(8)		Mn(36)		
2P	15.5	1.08							Fe(95)	
3P	12.9	0.92		Si(16)				Mn(65)		
4P	10.7	0.69		Si(35)		K(6)		Mn(33)		Zn(18)
5P	10.0	0.93						Mn(91)		
6P	9.2	1.77	Al(15)	Si(46)	S(8)					
7P	4.6	2.53		Si (12)	S(17)		Ca(39)	Mn(18)		
8P	3.5	1.43		Si(12)	S(11)				Fe(62)	
9P	3.3	1.95		Si(94)						
10P	2.6	0.98			S(44)		Ca(55)			
11P	1.9	2.26					Ca(90)			

Table 3 – Types of particles (% in brackets corresponds to relative mass composition; elements with Z<=8 were not considered) evidenced in deposition samples and roof dust collected at CCV using SEM-EDX after Hierarchical Cluster Analysis of 4 dataset containing the individual composition of 1000 particles, corresponding relative abundance (minimum and maximum values), mean diameter and attribution.

Cluster	Relative abundance (%)		Mean diameter (µm)	Composition							
	Deposition (n=3)	Roof dust (n=1)									
1D	12-41	29	24.8		Al(2)	Si(5)				Mn(77)	Fe(12)
2D	12-28	13	25.3	Mg(4)	Al(11)	Si(34)	S(2)	K(2)	Ca(26)	Mn(19)	
3D	12-18	20	19.9	Mg(3)	Al(8)	Si(18)	S(3)		Ca(4)	Mn(51)	Fe(10)
4D	10-27	19	13.4		Al(19)	Si(47)	S(2)	K(3)	Ca(5)	Mn(10)	Fe(9)
5D	0-9	0	33.9	Mg(4)	Al(7)	Si(21)		K(1)	Ca(27)	Mn(38)	
6D	4	7	23.7		Al(4)	Si(87)					
7D	2-3	2	13.0		Al(2)	Si(3)				Mn(2)	Fe(88)
8D	0-7	6	13.2		Al(10)	Si(21)	S(4)		Ca(4)	Mn(12)	Fe(38)
9D	0-2	0	14.6		Al(35)	Si(5)	S(6)		Ca(33)	Mn(10)	
10D	0-7	4	9.7	Mg(7)	Al(5)	Si(9)	S(6)		Ca(67)		

Table 4: Crystalline phases identified by X-ray Diffraction in PM_{10}, deposition (Dep) and roof dust (RD) samples collected at CROS and CCV sites (x = detected).

Crystalline Phase	Formula	Labels	PM samples						
			PM10a	PM10b	Depa	Depb	Depc	RDa<70µm	RDb (70-100µm)
Gypsum	$CaSO_4$, $2H_2O$	Gy	x	x					
Quartz	SiO_2	Q	x	x	x	x	x	x	x
Aluminum silicate	Al_2SiO_5	A	x						
Calcium carbonate	$CaCO_3$	Ca		x	x	x	x	x	x
Bixbyite	Mn_2O_3	Bi	x		x	x	x	x	x
Bixbyite	$FeMnO_3$	Bi			x	x	x	x	x
Manganese dioxide	MnO_2	M	x						
Rhodochrosite	$MnCO_3$	Rh		x	x	x	x	x	x
Manganosite or Iron manganese oxide	MnO or $(FeO)_{0.099}(MnO)_{0.901}$	Mo			x	x	x	x	x
Hausmannite	Mn_3O_4	Ha			x	x	x	x	x
Alabandite	MnS	S			x	x	x		
Dolomite	$CaMg(CO_3)_2$	D			x		x	x	
Bustamite	$CaMn(SiO_3)_2$	Bu							x
Hematite	Fe_2O_3	H							x
Magnetite	Fe_3O_4	F							x
Manganese iron silicon	Mn_4FeSi_3	Mi			x	x	x	x	x
Silicates (Glaucochroite or Kirschsteinite)	$(Ca,Mn)_2SiO_4$ $Ca(Fe,Mg)SiO_4$	Si			x	x			
Manganocalcite	$(Ca,Mn)CO_3$	Ma					x	x	
Microcline	$KAlSi_3O_8$	Mc					x	x	